APPLIED PHYSICS LETTERS **105**, 143109 (2014)

Direct observation of resistive heating at graphene wrinkles and grain boundaries

Kyle L. Grosse,[1] Vincent E. Dorgan,[2] David Estrada,[2,a)] Joshua D. Wood,[2,b)] Ivan Vlassiouk,[3] Gyula Eres,[4] Joseph W. Lyding,[2] William P. King,[1,5] and Eric Pop[2,6,c)]
[1]*Mechanical Science and Engineering, Univ. Illinois Urbana-Champaign, Urbana, Illinois 61801, USA*
[2]*Electrical and Computer Engineering, Univ. Illinois Urbana-Champaign, Urbana, Illinois 61801, USA*
[3]*Energy and Transportation Science Division, Oak Ridge National Laboratory, Oak Ridge, Tennessee 37831, USA*
[4]*Materials Science and Technology Division, Oak Ridge National Laboratory, Oak Ridge, Tennessee 37831, USA*
[5]*Materials Science and Engineering and Materials Research Laboratory, University of Illinois at Urbana-Champaign, Urbana, Illinois 61801, USA*
[6]*Electrical Engineering, Stanford University, Stanford, California 94305, USA*

(Received 25 July 2014; accepted 15 September 2014; published online 7 October 2014)

We directly measure the nanometer-scale temperature rise at wrinkles and grain boundaries (GBs) in functioning graphene devices by scanning Joule expansion microscopy with ~50 nm spatial and ~0.2 K temperature resolution. We observe a small temperature increase at select wrinkles and a large (~100 K) temperature increase at GBs between coalesced hexagonal grains. Comparisons of measurements with device simulations estimate the GB resistivity (8–150 Ω μm) among the lowest reported for graphene grown by chemical vapor deposition. An analytical model is developed, showing that GBs can experience highly localized resistive heating and temperature rise, most likely affecting the reliability of graphene devices. Our studies provide an unprecedented view of thermal effects surrounding nanoscale defects in nanomaterials such as graphene. © *2014 AIP Publishing LLC*. [http://dx.doi.org/10.1063/1.4896676]

Graphene, a monolayer of hexagonally arranged carbon atoms, has been the subject of intense research due to its thinness (~3.4 Å), unique linear band structure,[1] and quasi-ballistic electrical and thermal transport up to micron length scales at room temperature.[2,3] Graphene applications typically rely on material growth by chemical vapor deposition (CVD) on metal substrates.[4] This process can produce graphene up to meter dimensions,[5] but typically of a polycrystalline nature, with the sheet being made up of a patchwork of grains connected by grain boundaries (GBs).[6] In addition, various transfer processes from the metallic growth substrate onto other substrates (e.g., SiO_2, BN, and plastics) can lead to wrinkling of the monolayer material.[7] Not surprisingly, GBs and wrinkles are expected to degrade the thermal,[8] electrical,[9,10] and mechanical[11] properties of graphene. Recent work has measured the electrical resistance of graphene GBs,[9–14] which is important as they limit the overall electrical performance of graphene devices grown by CVD.[6] However, the associated temperature rise resulting from nanometer-scale resistive heating of GBs is currently unknown. Understanding this aspect is important both from a graphene device perspective (e.g. reliability) and also as a unique platform directly connecting the technology of nanoscale thermometry tools with the science of atomic-scale heat generation at defects within realistic devices.

In this study, we measured the nanometer-scale temperature rise in CVD grown hexagonal graphene grains using scanning Joule expansion microscopy (SJEM),[15–18] a thermometry technique based on atomic force microscopy (AFM). We specifically study the resistive heating at graphene wrinkles and GBs, giving insight into the coupled electrical and thermal properties of such nanoscale defects. We observe a small temperature rise at wrinkles and a larger temperature rise at GBs (150%–300% greater than the surrounding graphene) due to the finite GB resistivity and to non-uniform current flow across GBs, visualized here with nanometer-scale resolution.

Figure 1(a) shows the optical image of a typical GB device used in this study, labeled as Device 1. Sample fabrication is summarized below, while details can be found in the supplementary material[19] and in recent reports.[12,20–23] CVD graphene was grown by atmospheric pressure CVD (APCVD) on electropolished Cu foil.[12,20] Graphene was transferred[21] from the Cu foil to SiO_2 (90 nm) on Si (highly p-doped) substrates. Suitable grains and GBs were located by optical microscopy, and electrical contacts were accomplished by electron beam lithography and deposition of 1/70 nm Cr/Pd contacts.[23] Fabrication was completed by spin coating the samples with 55–70 nm of poly(methyl methacrylate) (PMMA), which amplifies the thermo-mechanical expansions of the graphene and GB device for the SJEM technique.[16–18]

Figure 1(b) shows the surface thermo-mechanical expansion Δh measured by SJEM overlaid onto the device topography during operation. A sinusoidal waveform with amplitude V_{DS} was applied to the device at frequency

a)Present address: Materials Science and Engineering, Boise State University, Boise, Idaho 83725, USA.
b)Present address: Materials Science and Engineering, Northwestern University, Evanston, Illinois 60208, USA.
c)Author to whom correspondence should be addressed. Electronic mail: epop@stanford.edu

 © 2014 AIP Publishing LLC

This article is copyrighted as indicated in the article. Reuse of AIP content is subject to the terms at: http://scitation.aip.org/termsconditions. Downloaded to IP: 171.66.208.130 On: Tue, 07 Oct 2014 19:49:55

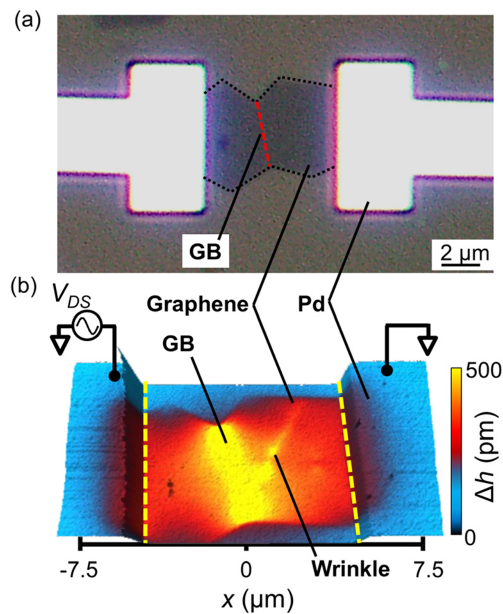

FIG. 1. (a) Optical image of Device 1 with two hexagonal graphene grains connected by a GB. The image has been adjusted to improve contrast. Light areas are the Pd electrodes and the substrate is SiO_2/Si. (b) Measured SJEM surface expansion Δh as a color overlay on the device topography with PMMA coating. SJEM operates by biasing the device with a sinusoidal voltage waveform with amplitude V_{DS} to resistively heat the device, and the AFM measures the resulting thermo-mechanical expansion of PMMA covering the device. The measured Δh is proportional to the device temperature rise ΔT and is related by a FEA model.[16,17]

$\omega = 61$–230 kHz. The AFM cantilever was in contact with the surface and a lock-in amplifier at 2ω, with a bandwidth of 4–125 Hz, recorded the peak-to-peak surface expansion Δh. (The supplementary material further discusses the SJEM technique.[19]) The spatial and temperature resolution of our SJEM measurements are ~50 nm and ~0.2 K, respectively, based on our previous reports.[16–18] The peak-to-peak graphene temperature rise ΔT is proportional to the measured Δh, and the two are related by finite element analysis (FEA) modeling.[16,17] The hexagonal graphene shape and GB are evident from the measured Δh in Figure 1. We also observe a decrease (increase) in Δh as the graphene device *laterally* expands (contracts) due to its hexagonal shape, creating a non-uniform current density throughout the device. The measured Δh increases 100%–200% at the GB near the device center ($x \approx 0\,\mu$m) compared to the graphene sheet due to (1) localized Joule heating from the presence of the GB with finite resistivity ρ_{GB} and (2) the laterally constricting device shape. The supplementary material discusses simulations which show <25% increase in Δh at the GB compared to device center due to the constricting graphene shape;[19] thus, we attribute the majority of the measured Δh increase to the GB resistivity ρ_{GB}. Figure 1(b) also reveals a local increase (~25%) in Δh at a wrinkle, discussed below.

Next, we turn to our AFM and SJEM measurements of a single-grain graphene device with wrinkles, but without a GB. Figures 2(a) and 2(b) show the measured Δh and second resonance amplitude A_2 of such a device. Figure 2(b) shows A_2 measurements from dual alternating contact AFM measurements. (The supplementary material describes the dual alternating contact AFM technique[19] which contrasts the graphene from the surrounding SiO_2.[24]) The labeled wrinkle in Fig. 2(b) has a height of 3–12 nm which varies along its length. We observe no increase in the measured thermal expansion along the wrinkle, and, therefore, we do not expect a large increase in ΔT at this wrinkle. This observation agrees with recent theoretical work suggesting that tall (>5 nm) wrinkles have low electrical resistance.[7] The measured thermo-mechanical expansion Δh at the contacts is due to current crowding at the graphene-metal interface.[16]

Figures 2(c) and 2(d) show the simulated Δh and ΔT for the single grain graphene device. A three-dimensional (3D) FEA model was used to interpret these SJEM measurements as described in the supplementary material.[19] The Fourier transform of the heat diffusion and Poisson equations

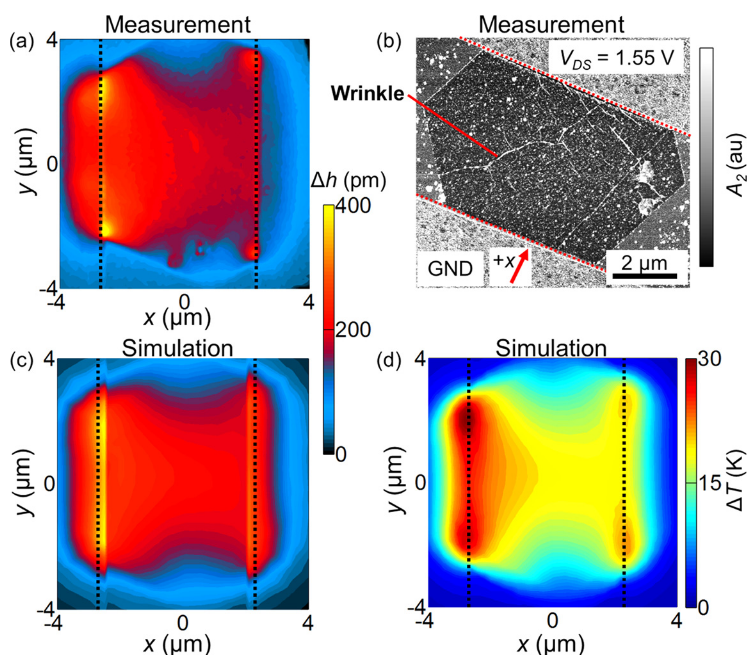

FIG. 2. (a) Measured Δh of single domain graphene device without a grain boundary. (b) Second resonance amplitude A_2 image of device, which is sensitive to the sample surface properties.[24] Wrinkles are seen as white lines across the graphene sheet, with one labeled for reference. The image is tilted counterclockwise by ~63° with respect to (a), and the red arrow shows the x-axis direction. Pd electrodes are shown with lighter contrast at the top-right and bottom-left. (c) and (d) Simulated thermal expansion Δh and temperature rise ΔT of the device.

This article is copyrighted as indicated in the article. Reuse of AIP content is subject to the terms at: http://scitation.aip.org/termsconditions. Downloaded to IP: 171.66.208.130 On: Tue, 07 Oct 2014 19:49:55

coupled with a thermo-mechanical model simulated the frequency response of Δh and ΔT. Fitting the measured and simulated Δh for two measurements each at $V_{DS} = 0.54$, 1.12, and 1.67 V yields the bulk graphene resistivity $\rho = 0.11 \pm 0.01\ \Omega\ \mu$m (sheet resistance[25] $R_S \approx 330\ \Omega$/sq) and graphene-metal contact resistivity[16] $\rho_C = 280 \pm 90\ \Omega\ \mu m^2$ (per unit area). These values are in-line with previous studies of monolayer graphene and graphene-metal contacts on SiO_2.[16,25] The model matches measurements with a coefficient of determination $r^2 = 0.78 \pm 0.06$ for all V_{DS} and yields a total device resistance $R = 388\ \Omega$, close to the measured 371 Ω. More information for fitting measurements and simulations is in the supplementary material.[19]

We now return to a more in-depth investigation of AFM and SJEM measurements of Device 1 which had a single GB. Figures 3(a) and 3(b) show the measured Δh and A_2 of two coalesced graphene grains, the same device with one GB as in Fig. 1. Figure 3(a) shows a large, 100%–200% increase in Δh at the GB. Figure 3(b) also reveals multiple wrinkles, most being 1–3 nm tall and oriented parallel to the current flow direction (along the x-axis). However, the wrinkles show no measureable increase in Δh in Fig. 3(a). We only measure a 25% increase in Δh at one wrinkle (2–3 nm tall), which rests at a ~56° angle to the current flow direction. However, the measured Δh is ~4–8 times larger at the GB than the wrinkle, indicating the GB has a greater (detrimental) influence on device performance. Figures S4 and S5 of the supplementary material show similar behavior for the measured Δh at wrinkles and GBs for two other devices.[19]

Figures 3(c) and 3(d) show the simulated Δh and ΔT for Device 1. Fitting the measured and simulated Δh for two measurements each at $V_{DS} = 0.56$, 1.13, 2.34, and 2.95 V yields bulk graphene resistivity $\rho = 8.3 \pm 0.1 \times 10^{-2}\ \Omega\ \mu$m (sheet resistance $R_S \approx 250\ \Omega$/sq), grain boundary resistance $\rho_{GB} = 120 \pm 60\ \Omega\ \mu$m, and graphene-contact resistivity $\rho_C = 30 \pm 10\ \Omega\ \mu m^2$. (The contact resistivity is underestimated, an artifact discussed in the supplementary material.[19])

The GB resistivity ρ_{GB} is commonly defined per unit width,[9–13] here the width of the GB being about 4.7 μm for Device 1. One can also define an effective GB length $\ell_{\text{eff}} = \rho_{GB}/R_S \approx 490$ nm for Device 1, corresponding to the length of graphene channel that would yield the same resistance as the GB.[13] (The longer the effective GB length, the larger the resistive contribution of the GB relative to the total resistance of the device.) Wrinkles were shown to have a small effect on Δh and were not included in the simulation. The model matches measurements well ($r^2 = 0.89 \pm 0.03$) and predicts the total device resistance $R = 481\ \Omega$, close to the measured value of 471 Ω. Figure 3(d) shows the simulated ΔT increases ~150% at the GB center and ~300% at the GB edge compared to the middle of the graphene grains. The ~150% rise is due to ρ_{GB}, and the ~300% rise is due to ρ_{GB} plus the additional effects of current crowding near the grain edges.

Table I summarizes the GB resistivity ρ_{GB} extracted from three devices in this study, compared to values reported in the literature.[9–13] The full range of ρ_{GB} is from ~8 to 43 000 Ω μm for GBs from CVD-grown graphene on Cu and transferred to SiO_2 substrates. By comparison, reported ρ_{GB} for graphene directly grown on SiC range from 7 to 100 Ω μm.[12,26] Although we observe a notable 150%–300% temperature increase at the GB, we estimate relatively low ρ_{GB} for our devices compared to the range reported in the literature for graphene grown by CVD on Cu and transferred for measurements to SiO_2. Our devices were grown using similar methods to those of Clark *et al.*[12] and we report similar ρ_{GB} as their study. Interestingly, the results summarized in Table I show no evident trend between graphene grain type and the electrical properties of GBs.[9–13]

In order to facilitate a simpler yet physical understanding of power dissipation at GBs, we developed an analytical model to predict their temperature rise for the range of observed ρ_{GB} in all studies summarized by Table I.[9–13] Figure 4(a) shows the model geometry and associated

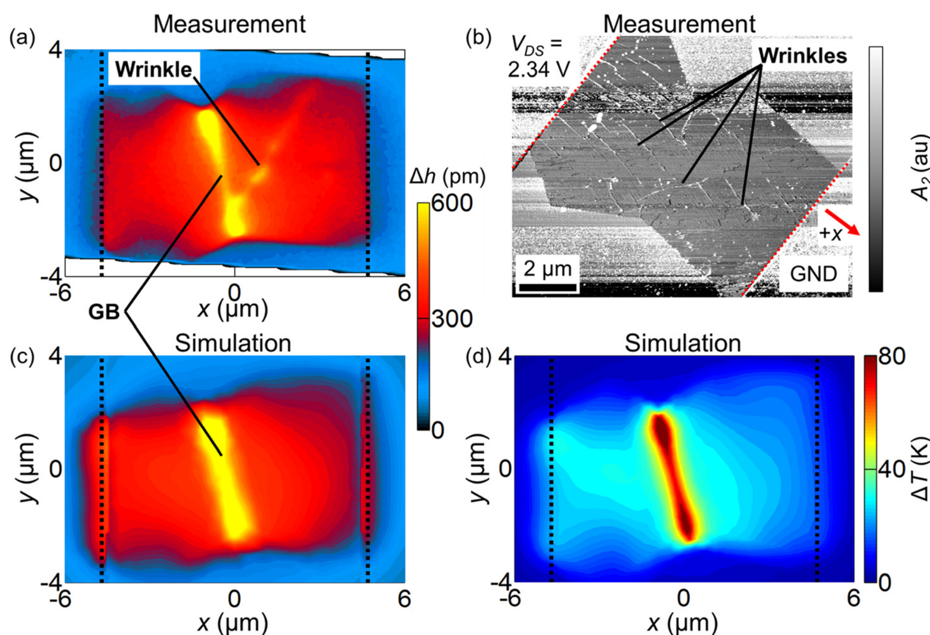

FIG. 3. (a) Measured Δh of Device 1 from Fig. 1. The large Δh measured at $x \approx 0\ \mu$m is due to Joule heating at the GB. Joule heating of a wrinkle is also evident. (b) Measured A_2 image of device, tilted clockwise by ~35° from (a). Red arrow shows x-axis direction and the Pd electrodes are shown with lighter contrast at the top-left and bottom-right. Wrinkles are evident as white lines across the graphene. (c) and (d) Simulated Δh and ΔT of the device, including only the GB which had stronger resistive heating than the wrinkles.

This article is copyrighted as indicated in the article. Reuse of AIP content is subject to the terms at: http://scitation.aip.org/termsconditions. Downloaded to IP: 171.66.208.130 On: Tue, 07 Oct 2014 19:49:55

TABLE I. Measured ρ_{GB} from three devices in this study and other values reported in the literature for graphene grown by CVD, sorted in approximate order of increasing GB resistivity. The measurement column lists the method used to estimate ρ_{GB}. AC-EFM is alternating current electrostatic force microscopy. Resistive measurements are direct electrical measurements of the grain resistance, and 4-probe scanning tunneling microscopy (STM) uses a combination of 4-probe measurements and scanning tunneling spectroscopy (STS) at the GB to measure ρ_{GB}. The GB of Device 2 did not experience significant heating and approached the resolution of our simulations and measurements (see supplementary material[19]).

Device or study	ρ_{GB} (Ω μm)	Measurement	Fabrication/grain notes
Device 2 (Fig. S4)	8 ± 8	This study	Electropolished Cu, APCVD, hexagonal grains
Device 1 (Fig. 3)	120 ± 60		
Device 3 (Fig. S5)	150 ± 30		
Huang[11]	<60	AC-EFM	LPCVD, dendritic/Flower patchwork grains
Clark[12]	43–140	4-Probe STM	Electropolished Cu
			APCVD, hexagonal grains
Tsen[13]	650–3200	Resistive	LPCVD (2 Torr)
			Patchwork grains
	12 900–43 000	Resistive	Formed Cu pocket,[32]
			LPCVD (2 Torr), dendritic / flower grains
Yu[9]	8400	Resistive	APCVD, hexagonal grains
Jauregui[10]	2000–15 000	Resistive	APCVD, hexagonal grains

electrostatic and thermal boundary conditions. The steady-state analytical model is different from our frequency-dependent measurements and FEA predictions. The solution to the electrostatics and heat diffusion problems with accompanying assumptions is provided in the supplementary material and was verified by an FEA model.[19] For the analysis described below, we assume graphene properties similar to Device 1 with a channel length $2L = 10\,\mu$m. Figure 4(b) shows the predicted voltage $V(x)$ and temperature $T(x)$ profile of the device schematic from Fig. 4(a). The model predicts that the small voltage drop across the GB (V_{GB}) causes a large localized temperature rise (T_{GB}) due to the highly confined Joule heating at the grain boundary. Figure 4(c) shows the percent voltage drop $V_{\%} = V_{GB}/V_0$ and percent power dissipated $P_{\%} = P_{GB}/P_0$ at the GB for the geometry shown in Figure 4(a), where V_0 and P_0 are the total applied voltage and power dissipation of the entire device. Current continuity along the device yields $V_{\%} = P_{\%}$. We estimate $V_{\%} = P_{\%} = 2.9\%$ for Device 1 shown in Fig. 3.

Figure 4(c) shows the predicted temperature ratio between the GB and the rest of the graphene grain, $T_{\%} = T_{GB}/T(L/2)$, from the analytical model; here, the graphene temperature is taken at $x = L/2$, the halfway point between the GB and contacts. The analytical model overestimates $T_{\%}$ by 20%–50% compared to FEA simulations, as it does not account for the (two-dimensional) heat spreading through the substrate at the GB. The analytical model predicts $T_{\%} \approx 300\%$ for Device 1, close to the observed value of 150%–300%. In fact, the GB dominates the temperature rise ($T_{\%} > 200\%$) of Device 1 for any value $\rho_{GB} > 60\ \Omega\ \mu$m, yet the associated $V_{\%} = P_{\%} = 1.6\%$ because the GB is a highly localized heat source versus the $10\,\mu$m long device. These results suggest that, in relatively "large" (e.g., $> 5\,\mu$m) interconnects with micron-size grains, GBs may not significantly affect electrical performance, but the GBs will dominate the temperature rise at such "hot spots" and therefore limit the interconnect reliability. A similarly small effect of GBs on large graphene interconnects has been predicted for their thermal conductivity,[8] as long as grains are micron-size (or

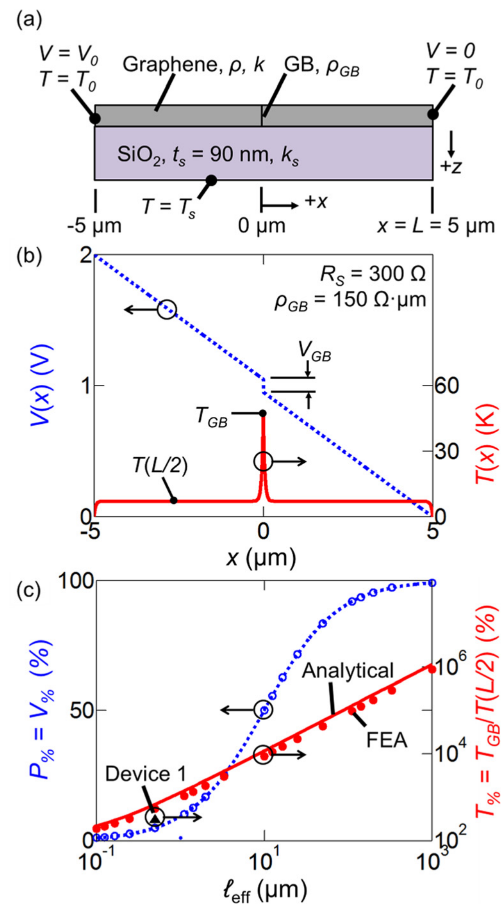

FIG. 4. (a) Schematic for the GB analytical model, showing two graphene domains ($L = 5\,\mu$m) on 90 nm SiO_2 with a GB at the center ($x = 0\,\mu$m). The contacts are biased at $V = V_0$ (left) and $V = 0$ (right). (b) Analytically modeled voltage $V(x)$ and temperature $T(x)$ of a device with similar physical characteristics as Device 1. The figure shows the GB voltage drop V_{GB} and temperature rise T_{GB}. (c) Predicted percent voltage drop $V_{\%}$ and power dissipation $P_{\%}$ at the GB and predicted percent GB temperature rise $T_{\%}$ relative to the graphene sheet. The effective GB length ℓ_{eff} is the length of the graphene channel with the same resistance as the GB.[13] Lines and markers are obtained with the analytical and FEA models, respectively. The black triangle marker is the measured $T_{\%}$ of Device 1. More information on the model is provided in the supplementary material.[19]

This article is copyrighted as indicated in the article. Reuse of AIP content is subject to the terms at: http://scitation.aip.org/termsconditions. Downloaded to IP: 171.66.208.130 On: Tue, 07 Oct 2014 19:49:55

larger), i.e., greater than the graphene phonon mean free path which is of the order of 100s of nm.[3]

In order to understand the effect of GB temperature rise on "small" (e.g., $<1\ \mu$m) graphene devices and interconnects we recall recent experiments which have shown that GBs perturb the electronic wave functions for <10 nm of the surrounding graphene.[27] The electron-phonon scattering mean free path is also of the order 20–80 nm in graphene on SiO_2 at room temperature.[25] These two length scales suggest that resistive heating only occurs within a few tens of nanometers from the GB itself. However, the length scale of heat *flow* (1/*e* temperature decay) away from the GB heat source is the lateral thermal healing length, $L_H \approx 0.1$–$0.2\ \mu$m for graphene on common SiO_2 (90–300 nm) substrates on Si.[19,28,29] Thus, the average temperature of a sub-micron graphene device with even a single GB will be significantly affected by the local power dissipation at the GB.

In both small and large graphene devices and interconnects with GBs, the temperature rise at such highly localized nanoscale defects could lead to premature device failure[29] before the *average* temperature of the graphene sheet has significantly increased. Both graphene oxidation or dielectric breakdown may be more likely to occur at GBs. These scenarios are similar to carbon nanotube (CNT) devices, where breakdown[30] and highly localized temperature rise at nanoscale defects have also been studied with SJEM.[18]

In conclusion, we directly observed nanometer-scale Joule heating of CVD-grown graphene using SJEM with $\sim$50 nm and $\sim$0.2 K spatial and temperature resolution. We noted a small increase in temperature at some wrinkles but a large 150%–300% increase in temperature at GBs. Comparing SJEM and electrical measurements with simulations we estimate $\rho_{GB} = 8$–$150\ \Omega\ \mu$m for our devices, among the lowest values reported for CVD graphene.[9–13] An analytical model is developed to predict power dissipation, voltage drop, and temperature rise at GBs for the range of ρ_{GB} reported in the literature. The model predicts that the GB may experience a large localized temperature rise which could lead to localized device or dielectric failure at GB locations, even before a significant increase of the average device temperature.

Finally, methods which measure nanometer-scale temperatures, such as SJEM and SThM (scanning thermal microscopy), have greater sensitivity to study graphene GBs than electrical techniques alone due to the large and localized temperature rise at GBs and similar atomic-scale defects. Knowledge of the nanoscale temperature rise and Joule heating at graphene GBs is important for understanding graphene devices and their reliability, as well as the physics of polycrystalline graphene sensors, which have increased sensitivity at their GBs and defects.[6,31]

The authors gratefully acknowledge the help of J. C. Koepke. This work was supported in part by the National Science Foundation (NSF) Grant Nos. ECCS 1002026 and ECSS 1201982, the National Defense Science and Engineering Graduate Fellowship (D.E. and J.D.W.), and the Army Research Office (ARO) Grant No. PECASE W911NF-11-1-0066 (E.P.). The synthesis science performed at ORNL by G.E. was sponsored by the Materials Sciences and Engineering Division, Office of Basic Energy Sciences, U.S. Department of Energy (DOE). Research on graphene synthesis performed by I.V. was sponsored by the Laboratory Directed Research and Development Program of ORNL, managed by UT-Battelle, LLC, for the U.S. DOE.

[1]A. K. Geim and K. S. Novoselov, Nat. Mater. **6**, 183 (2007); S. D. Sarma *et al.*, Rev. Mod. Phys **83**, 407 (2011).
[2]A. S. Mayorov *et al.*, Nano Lett. **11**, 2396 (2011).
[3]M.-H. Bae *et al.*, Nat. Commun. **4**, 1734 (2013).
[4]X. Li *et al.*, Science **324**, 1312 (2009).
[5]S. Bae *et al.*, Nat. Nanotechnol. **5**, 574 (2010).
[6]A. W. Cummings *et al.*, Adv. Mater. **26**, 5079–5094 (2014).
[7]W. Zhu *et al.*, Nano Lett. **12**, 3431 (2012).
[8]A. Y. Serov, Z.-Y. Ong, and E. Pop, Appl. Phys. Lett. **102**, 033104 (2013).
[9]Q. Yu *et al.*, Nat. Mater. **10**, 443 (2011).
[10]L. A. Jauregui *et al.*, Solid State Commun. **151**, 1100 (2011).
[11]P. Y. Huang *et al.*, Nature **469**, 389 (2011).
[12]K. W. Clark *et al.*, ACS Nano **7**, 7956 (2013).
[13]A. W. Tsen *et al.*, Science **336**, 1143 (2012).
[14]M. Ahmad *et al.*, Nanotechnology **23**, 285705 (2012); L. Tapasztó *et al.*, Appl. Phys. Lett. **100**, 053114 (2012); H. Zhang *et al.*, J. Phys. Chem. C **118**, 2338 (2014).
[15]J. Varesi and A. Majumdar, Appl. Phys. Lett. **72**, 37 (1998).
[16]K. L. Grosse *et al.*, Nat. Nanotechnol. **6**, 287 (2011).
[17]K. L. Grosse *et al.*, Appl. Phys. Lett. **102**, 193503 (2013).
[18]X. Xie *et al.*, ACS Nano **6**, 10267 (2012).
[19]See supplementary material at http://dx.doi.org/10.1063/1.4896676 for details on device fabrication, SJEM, Joule heating due to GB geometry, FEA model, AFM measurements, other devices, the analytical model, and thermometry of GBs.
[20]I. Vlassiouk *et al.*, Carbon **54**, 58 (2013).
[21]X. Liang *et al.*, ACS Nano **5**, 9144 (2011).
[22]Y. Dan *et al.*, Nano Lett. **9**, 1472 (2009).
[23]V. E. Dorgan *et al.*, Nano Lett. **13**, 4581 (2013).
[24]B. Jabakhanji *et al.*, Phys. Rev. B **89**, 085422 (2014); N. F. Martinez *et al.*, Appl. Phys. Lett. **89**, 153115 (2006).
[25]M.-H. Bae *et al.*, ACS Nano **5**, 7936 (2011).
[26]S.-H. Ji *et al.*, Nat. Mater. **11**, 114 (2012).
[27]J. C. Koepke *et al.*, ACS Nano **7**, 75–86 (2013).
[28]M.-H. Bae *et al.*, Nano Lett. **10**, 4787 (2010).
[29]A. Behnam *et al.*, Nano Lett. **12**, 4424 (2012).
[30]A. Liao *et al.*, Phys. Rev. B **82**, 205406 (2010).
[31]A. Salehi-Khojin *et al.*, Adv. Mater. **24**, 53 (2012).
[32]X. Li *et al.*, J. Am. Chem. Soc. **133**, 2816 (2011).

This article is copyrighted as indicated in the article. Reuse of AIP content is subject to the terms at: http://scitation.aip.org/termsconditions. Downloaded to IP: 171.66.208.130 On: Tue, 07 Oct 2014 19:49:55

Supporting Online Materials for

Direct observation of resistive heating at graphene wrinkles and grain boundaries

By: Kyle L. Grosse, Vincent E. Dorgan, David Estrada, Joshua D. Wood, Ivan Vlassiouk, Gyula Eres, Joseph W. Lyding, William P. King, and Eric Pop

I. Graphene Fabrication

Graphene was grown on 125 μm thick Cu foil by atmospheric pressure chemical vapor deposition (APCVD) similar to previous reports.[1,2] The Cu foil was electropolished in concentrated H_3PO_4, and the foils were then annealed for 1 hour at 1000 °C under 500 sccm flow of 2.5% H_2 in Ar. The growth was performed by addition of 8 sccm 0.1% CH_4 for 90 min.[1,2]

Graphene was transferred to the 90 nm SiO_2/Si substrates by coating one side of the Cu foil with a bilayer of poly(methyl methacrylate) (PMMA), 495 K A2 and 950 K A4, at 3000 rpm followed by a 200 °C bake for 2 min. An O_2 plasma etch of the graphene backside is performed prior to overnight exposure to the Cu etchant (Transene CE-100). The resultant PMMA/graphene film is transferred to a series of rinses to remove residual metal particles and etchants.[3] The film is then transferred onto the receiving substrate and left to dry in ambient conditions before removing the supporting PMMA in a 1:1 methylene chloride to methanol solution for 20 min. As a final step, the samples undergo a 400 °C anneal under 500 sccm Ar and 100 sccm H_2 flow to remove residual PMMA.[4]

Electron beam (e-beam) lithography was used to pattern contacts for the graphene devices. Suitable devices were located using optical microscopy to find isolated hexagonal graphene grains which coalesced forming a grain boundary (GB). First, e-beam lithography was used to pattern a region around each lead to remove undesired graphene by O_2 plasma etching. Then, e-beam lithography was used to pattern electrical contacts. Electrical contacts were deposited by e-beam evaporation of 1/70 nm of Cr/Pd. Fabrication was completed by spin coating the samples with 55-70 nm of PMMA for the scanning Joule expansion microscopy (SJEM) measurement.[5,6]

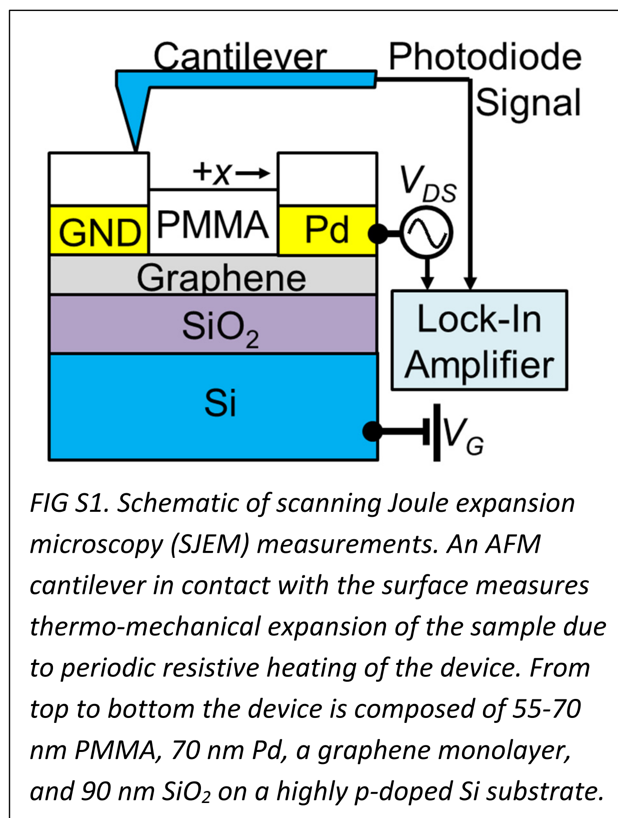

FIG S1. Schematic of scanning Joule expansion microscopy (SJEM) measurements. An AFM cantilever in contact with the surface measures thermo-mechanical expansion of the sample due to periodic resistive heating of the device. From top to bottom the device is composed of 55-70 nm PMMA, 70 nm Pd, a graphene monolayer, and 90 nm SiO_2 on a highly p-doped Si substrate.

II. Scanning Joule Expansion Microscopy (SJEM)

Figure S1 shows a schematic of the SJEM experiment. A sinusoidal waveform with amplitude V_{DS} biases the device and

generates resistive heating within the device. The resulting thermo-mechanical expansions of the sample were measured by the AFM cantilever, laser, and photodiode. A lock-in amplifier recorded the peak-to-peak (twice the amplitude) surface expansion Δh. A constant back-gate voltage $V_G = 0$ V was applied to control the carrier concentration of the graphene sheet during the measurements.

III. Joule Heating due to Grain Boundary (GB) Geometry

Figure S2 shows the simulated Δh and ΔT of Device 1 due to the device geometry and the presence of a grain boundary with finite resistivity $\rho_{GB} \neq 0$. The constriction of the graphene grains at the GB causes an increase in current density and Joule heating at the GB. Figures S2 (a) and (b) show the increased current density at the GB causes <25 % and <50 % increase in the simulated Δh and ΔT at the GB compared to the graphene sheet. The simulated V_{DS} for Figs. S2(a) and (b) was decreased to account for the lack of simulated grain resistance. Figures S2(c) and (d) show the same device with a resistive GB and show a 100-200 % and 150-300 % increase in the simulated Δh and ΔT at the GB, relative to the graphene sheet. The additional simulated increase in Δh and ΔT of Figs. S2(c) and (d) compared to Fig. S2(a) and (b) is due to the presence of a resistive GB. The simulated $\rho_{GB} = 180$ Ω µm was obtained from fitting measurements and simulations of Device 1 at $V_{DS} = 2.34$ V, shown in Fig. 3. Fitting measurements and simulation at other bias conditions yielded $\rho_{GB} =$ 60-180 Ω µm with the average and deviation of the simulated ρ_{GB} reported in Table I of the main text.

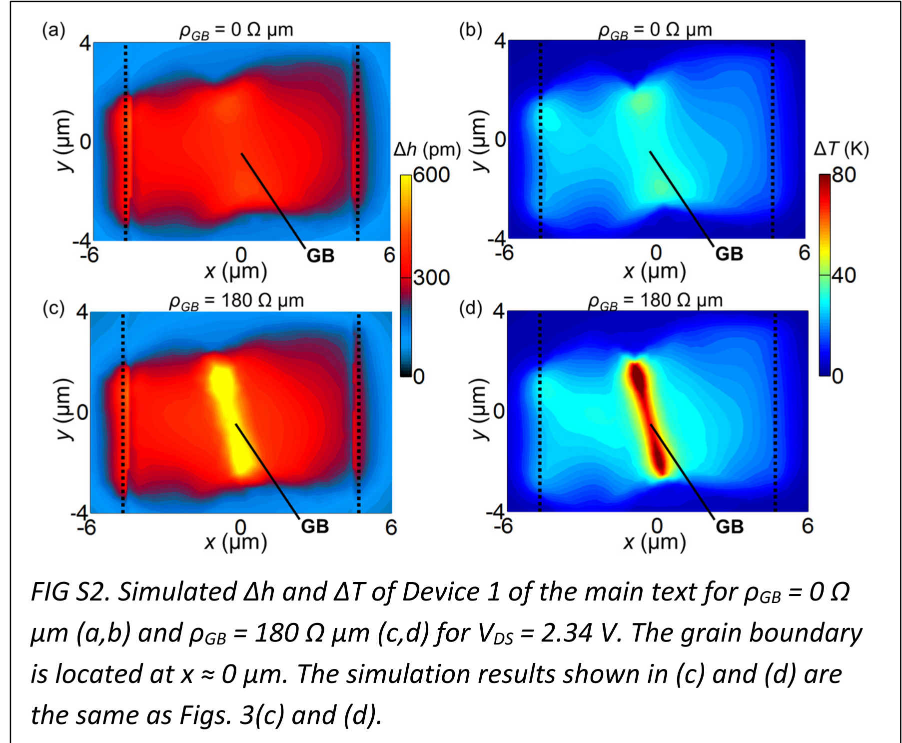

FIG S2. Simulated Δh and ΔT of Device 1 of the main text for $\rho_{GB} = 0$ Ω µm (a,b) and $\rho_{GB} = 180$ Ω µm (c,d) for $V_{DS} = 2.34$ V. The grain boundary is located at $x \approx 0$ µm. The simulation results shown in (c) and (d) are the same as Figs. 3(c) and (d).

IV. Finite Element Analysis Model

IV-A. Model Equations

A three dimensional (3D) frequency domain electro-thermo-mechanical finite element analysis (FEA) model was developed to simulate graphene device behavior. The heat diffusion and Poisson equations are shown in Eqs. S1 and S2.[7]

$$\rho_d c_P \frac{\partial T}{\partial t} = \nabla k \nabla T + \sigma (\nabla V)^2 \quad \text{(S1)}$$

$$\nabla \sigma \nabla V = 0 \quad \text{(S2)}$$

The density, heat capacity, thermal conductivity, electrical conductivity, temperature, and voltage are given by ρ_d, c_P, k, σ, T, and V. Equations S3 and S4 show the expected voltage and thermal waveforms.

$$V = V_{0\omega} + V_{1\omega}\cos(2\pi\omega t) \quad \text{(S3)}$$

$$T = T_{0\omega} + T_{1\omega}\cos(2\pi\omega t) + T_{2\omega}\cos(2\pi 2\omega t) \quad \text{(S4)}$$

The subscripts denote the amplitude of V and T at the zero, first, and second harmonics. The frequency of the applied bias ω = 61-230 kHz for all experiments. The peak-to-peak graphene temperature rise is $\Delta T = 2|T_{2\omega}|$. We applied $V_{0\omega}$ = 0 V which implies $T_{1\omega}$ = 0 K for a Joule heated device. The Fourier transform of Eqs. S1 and S2 with Eqs. S3 and S4 yields Eq. S5.

$$\nabla\begin{bmatrix} k & 0 & 0 & 0 & 0 \\ 0 & k & 0 & 0 & 0 \\ 0 & 0 & k & 0 & 0 \\ 0 & 0 & 0 & \sigma & 0 \\ 0 & 0 & 0 & 0 & \sigma \end{bmatrix}\nabla\begin{bmatrix} T_{0\omega} \\ T_{1\omega} \\ T_{2\omega} \\ V_{0\omega} \\ V_{1\omega} \end{bmatrix} = -\begin{bmatrix} \sigma(\nabla V_{0\omega})^2 + 0.5\sigma(\nabla V_{1\omega})^2 \\ 2\sigma(\nabla V_{1\omega}\nabla V_{0\omega}) - i\pi\rho_d c_P T_{1\omega}\omega \\ 0.5\sigma(\nabla V_{1\omega})^2 - i\pi\rho_d c_P T_{2\omega}2\omega \\ 0 \\ 0 \end{bmatrix} \quad \text{(S5)}$$

Equation S5 was coded into the PDE physics and coupled with thermo-mechanical physics in COMSOL. Transforming and solving the equations in the frequency domain reduced computation time and convergence issues.[6]

IV-B. Model Geometry

Figure S3 shows the 3D FEA model geometry. Device geometry was modeled from optical images and the e-beam lithography pattern of the device. The model consisted of 55-70 nm PMMA, 70 nm Pd, 1 nm graphene, and 90 nm SiO_2 on top of a 200 µm diameter, 100 µm tall Si cylinder. The large domain was chosen to be larger than the Si thermal penetration length.[6] The graphene was modeled 1 nm thick to decrease computation time, and all graphene properties were adjusted by the graphene thickness. The thermal properties of the graphene do not significantly affect the simulations.[5,6] The minimum mesh size was ~100 nm, larger than the measurement resolution.

Table S1 lists the thermophysical properties used in the model. We set the electrode resistivity to zero for the current model. Therefore, the FEA model directly

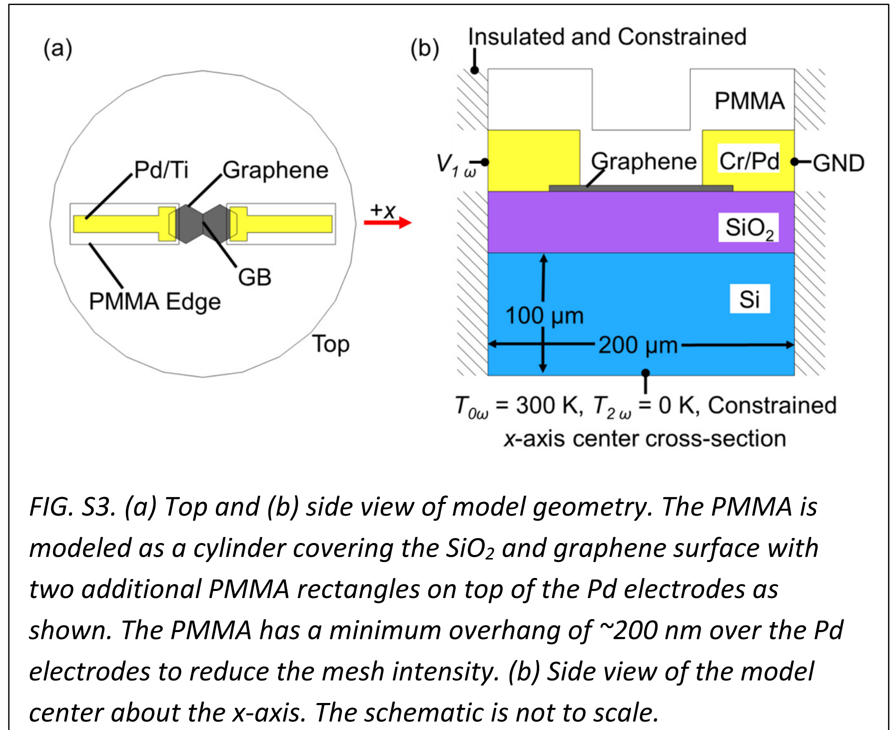

FIG. S3. (a) Top and (b) side view of model geometry. The PMMA is modeled as a cylinder covering the SiO_2 and graphene surface with two additional PMMA rectangles on top of the Pd electrodes as shown. The PMMA has a minimum overhang of ~200 nm over the Pd electrodes to reduce the mesh intensity. (b) Side view of the model center about the x-axis. The schematic is not to scale.

simulated the device resistance R, without simulating additional lead resistance. The model does not include the effects of wrinkles or temperature dependent graphene properties.

Table SI. Electro-thermo-physical properties of materials used in the simulation. From left to right the listed properties are the thermal conductivity, density, heat capacity, coefficient of thermal expansion, Poisson's ratio, and elastic modulus.

Material	k W m^{-1} K^{-1}	ρ_d kg m^{-3}	c_P J kg^{-1} K^{-1}	α_{CTE} K^{-1} ×10^6	v	E GPa
Graphene	300	2,100	710	-5	0.2	1000
Pd	30	12,000	244	11.8	0.39	121
PMMA	0.18	1,200	1,500	50	0.35	3
SiO_2	1.4	2,220	745	0.5	0.17	64
Si	80	2,330	712	2.6	0.28	165

Figure S3 also shows the boundary conditions for the 3D FEA model. The device is biased at the contacts and has a heat sink at the bottom as shown. The top surfaces are not mechanically constrained. All other surfaces are electrically and thermally insulated and mechanically constrained.

IV-C. Fitting Measurements and Simulations

Fitting FEA simulations and SJEM measurements of Δh yielded the graphene device properties and temperature rise. The model varied the graphene resistivity ρ, graphene-Pd contact resistivity ρ_C (per unit contact area) and GB resistance ρ_{GB} (per unit GB width). The best fit between measurements and simulations was found by the largest coefficient of determination r^2 (typically > 0.75) between measured and simulated Δh with a simulated device resistance R similar to measurements.

The measured graphene resistance R and voltage drop V_{DS} was calculated from two terminal resistance measurements. We calculated and subtracted the resistance and voltage drop of the Pd leads from the two terminal measurements. We prepared two sets of samples, and we found the Pd resistivity of each to be ~2.5×10^{-7} and ~5.0×10^{-7} Ω m, similar to our previous work.[5,8] Devices with higher resistivity Pd leads had higher simulated ρ_C indicating low quality Pd. We note that varying the Pd thermal conductivity between 15-30 W m^{-1} K^{-1}, calculated from the Wiedemann-Franz law, did not significantly change the simulations. The model did not account for wrinkles or temperature dependent graphene resistivity. Unknown probe resistance and contact resistance of our home-built atomic force microscopy (AFM) probe station introduced additional uncertainty in our measurements. Therefore, we adjusted the simulated Δh by -20 to +10 % depending on the device and bias condition to account for these discrepancies.

IV-D. Contact Resistivity Underestimation

The FEA simulations underestimate the graphene-Pd contact resistivity ρ_C due to inexact modeling of the graphene-Pd contact shape, which is tapered not rectangular, owing to the shape of the grains. Optical measurements were used to estimate the graphene shape for the FEA models; the limited resolution of this approach before Pd deposition may have led us to under-estimate the area of graphene under the contacts in the FEA model, which increases the simulated current crowding and contact heating. We also assume the PMMA has a square,

stepped profile at the Pd edge, instead of the measured conformal PMMA coating. Therefore, we simulate a thicker PMMA layer at the Pd edge. Figure S3 shows we model a 200 nm thick overhang of PMMA at the electrode edge, which is larger than the ~100 nm thick PMMA overhang experimentally observed.[5] We were unable to simulate a thinner PMMA overhang. The thicker PMMA layer at the Pd edge would increase the simulated Δh at the contacts. The inaccurate modeling of the graphene shape and PMMA coating at the contacts would increase the simulated contact heating and Δh at the contacts. Therefore, a lower than expected ρ_C (per unit area) could match the measured contact heating and Δh at the contacts. However, the simulated contact resistance did not significantly affect the simulated device resistance.

V. Dual Alternating Contact AFM Measurements

Dual alternating contact, or bimodal, AFM measurements can enhance the material contrast of an AFM image due to changes in surface mechanical properties.[9] The AFM cantilever is excited at the first and second resonances. The amplitude of the first resonance is held constant and used in the AFM feed-back loop to measure sample topography. The second resonance amplitude A_2 and its phase are recorded as the AFM cantilever raster scans the surface. Previous work has shown the second resonance has increased sensitivity to surface mechanical properties[9] and can identify monolayer from bilayer graphene.[10] In this study we post-process our AFM data by subtracting the average SiO_2 A_2 signal from each line scan. This process improves the image contrast and creates a uniform image by adjusting for changes of the AFM cantilever tip due to interaction with debris or tip wear while scanning.

VI. Additional Devices

VI-A. Device 2

Figures S4(a) and (b) show the measured Δh and A_2 of two coalesced graphene grains, Device 2. The analysis of Device 2 is similar to Device 1 of the main text and duplicate details are omitted here. Figure S4(a) shows a ~10-50 % increase in Δh at the GB. An increase in Δh of ~10-40 % is measured along two (1-2 nm tall) labeled wrinkles in Fig. S4(a). The two wrinkles rest at an angle 51 and 79 ° to the carrier flow direction (along the x-axis). We do not observe an increase in Δh at other wrinkles (1-4 nm tall) oriented parallel to the

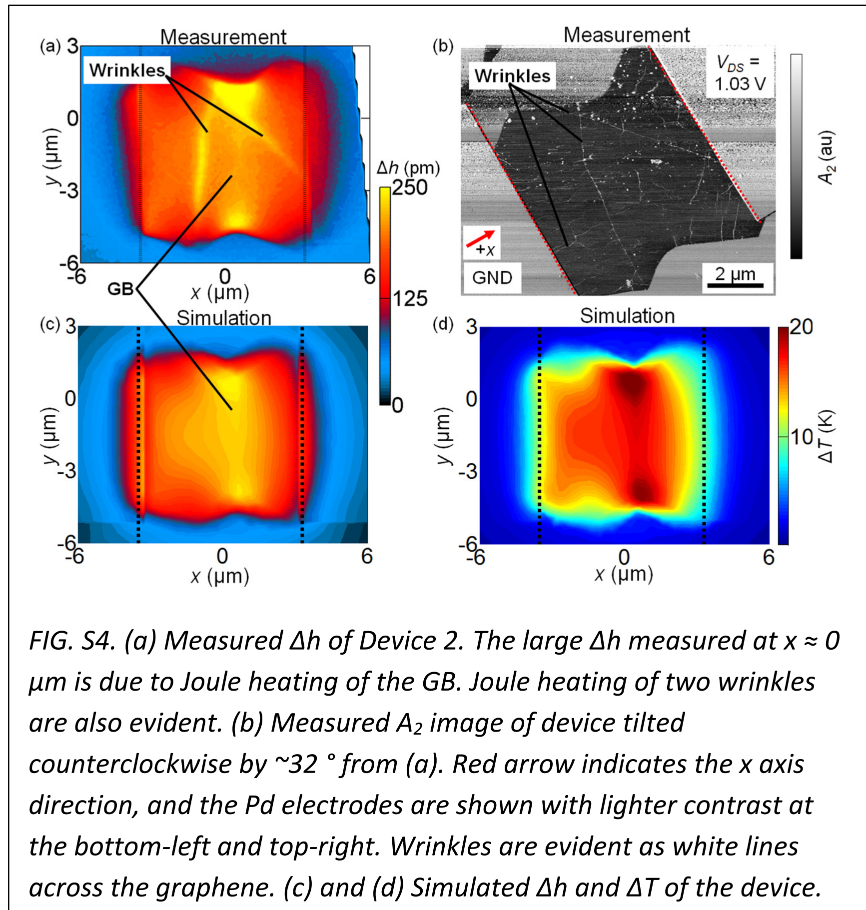

FIG. S4. (a) Measured Δh of Device 2. The large Δh measured at x ≈ 0 μm is due to Joule heating of the GB. Joule heating of two wrinkles are also evident. (b) Measured A_2 image of device tilted counterclockwise by ~32 ° from (a). Red arrow indicates the x axis direction, and the Pd electrodes are shown with lighter contrast at the bottom-left and top-right. Wrinkles are evident as white lines across the graphene. (c) and (d) Simulated Δh and ΔT of the device.

current flow direction.

Figures S4(c) and (d) show the simulated Δh and ΔT for Device 2. Fitting the measured and simulated Δh for two measurements each at V_{DS} = 0.35, 0.47, 1.03, and 1.72 V yields $\rho = 6.3 \pm 0.8 \times 10^{-2}$ Ω µm ($R_S \approx 190$ Ω/sq.), ρ_{GB} = 8 ± 8 Ω µm, and ρ_C = 25 ± 10 Ω µm^2. The model matches simulations with a coefficient of determination $r^2 = 0.89 \pm 0.02$ and simulates the device resistance R = 213 Ω, close to the measured 196 Ω. Figure S4(d) shows the simulated ΔT increases ~10-30 % at the GB.

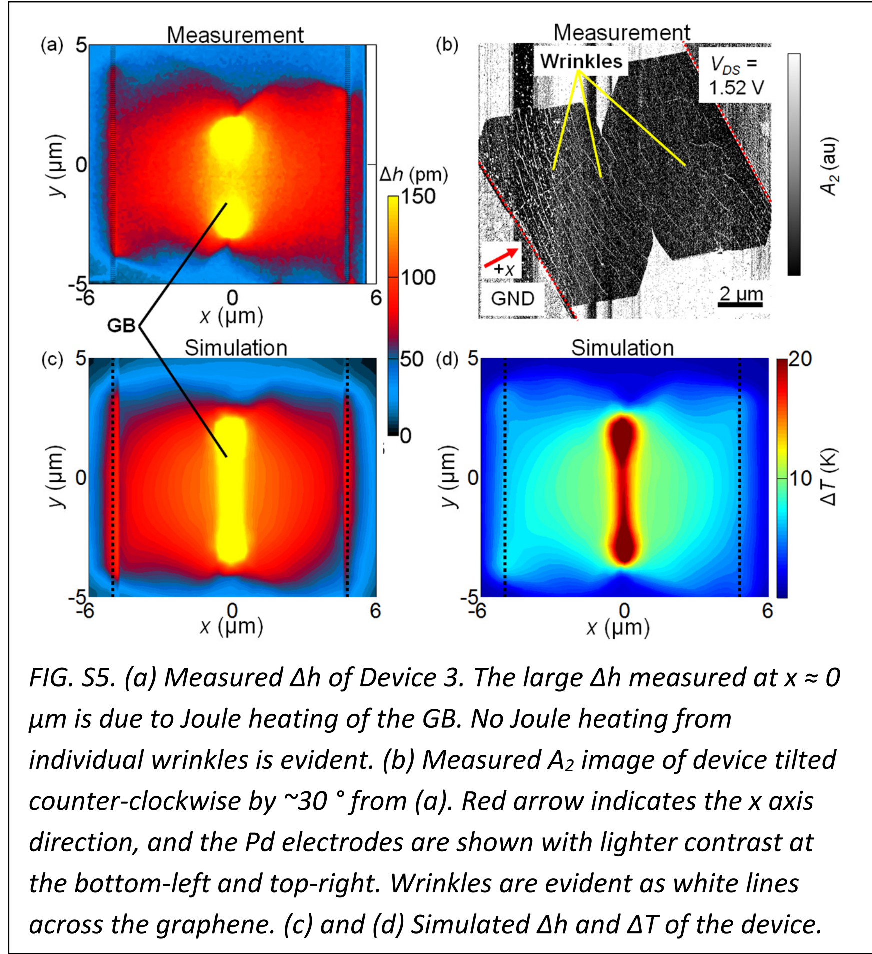

FIG. S5. (a) Measured Δh of Device 3. The large Δh measured at x ≈ 0 µm is due to Joule heating of the GB. No Joule heating from individual wrinkles is evident. (b) Measured A_2 image of device tilted counter-clockwise by ~30 ° from (a). Red arrow indicates the x axis direction, and the Pd electrodes are shown with lighter contrast at the bottom-left and top-right. Wrinkles are evident as white lines across the graphene. (c) and (d) Simulated Δh and ΔT of the device.

VI-B. Device 3

Figures S5(a) and (b) show the measured Δh and A_2 of two coalesced graphene grains, Device 3. The analysis of Device 3 is similar to Device 1 of the main text and repeated details are omitted here. Figure S5(a) shows a large 50-300 % increase in Δh at the GB. Figure S5(b) shows multiple wrinkles (1-6 nm tall) orientated perpendicular to the current flow direction (along the x-axis). No increase in Δh is observed at each wrinkle. However, the high wrinkle density makes it difficult to discern if all or none of the wrinkles experience uniform heating.

Figures S5(c) and (d) show the simulated Δh and ΔT for Device 3. Fitting the measured and simulated Δh for two measurements each at V_{DS} = 0.95, 1.45, and 1.9 V yields $\rho = 0.1 \pm 0.01$ Ω µm ($R_S \approx 300$ Ω/sq.), ρ_{GB} = 150 ± 30 Ω µm, and ρ_C = 130 ± 25 Ω µm^2. The model simulates ΔT increases ~100-300 % at the GB. We note the model under estimates Δh, and therefore ΔT, at the GB edges due to the limited (~100 nm) mesh resolution, and we expect the actual ΔT to be larger than FEA simulations.

VII. Analytical Model

VII-A. Derivation

A two dimensional (2D) analytical model was developed to predict the temperature rise and power dissipation for the range of observed ρ_{GB} (~10-10^4 Ω µm).[1,11,12,13] Figure 4(a) shows the model geometry and associated electrostatic and thermal boundary conditions. The analytical model assumes the device is uniform in width and does not capture the non-uniform current

density observed experimentally**.** The analytical model is a steady-state model and differs from our previously derived frequency domain FEA model used to interpret SJEM results. Solving the electrostatic component of Fig. 4(a) for the voltage profile $V(x)$ yields Eq. S6:

$$V(x) = \begin{cases} E*(L+\ell_{eff}-x) \text{ for } x<0 \\ E*(L-x) \text{ for } x>0 \end{cases} \tag{S6}$$

where $E = V_0 / (2L + \ell_{eff})$ and $\ell_{eff} = \rho_{GB}/R_S$. The effective GB length ℓ_{eff} is the length of the graphene channel with resistance equal to that of the GB.[13]

The percent voltage drop and power dissipated at the GB relative to the whole device are given by $V_{\%} = V_{GB}/V_0$ and $P_{\%}$. The voltage drop across the GB is $V_{GB} = V(0^-)-V(0^+)$, and the voltage drop across the entire device is V_0. The power dissipated at any point is given by $P(x) = V(x)\times I$, where I is the current. The constant (continuous) current density in the device implies $V_{\%} = P_{\%}$. Equation S7 shows a simple relation for $P_{\%}$, $V_{\%}$, ℓ_{eff}, and the device length $2L$.

$$P_{\%} = V_{\%} = 100/(1+2L/\ell_{eff}) \tag{S7}$$

Equation S8 shows the associated temperature rise profile $T(x)$ for the device voltage profile from Equation S6. Equation S8 is derived assuming the graphene is isothermal along its width and heat flows 1D (vertical) in the substrate to the heat sink at T_s.

$$\Theta(x) = \frac{\cosh(x/L_H)}{\cosh(L/L_H)} + \frac{Q_{GB}L_H}{2}\left[\tanh(L/L_H)\cosh(x/L_H) \pm \sinh(x/L_H)\right] \tag{S8}$$

The ± sign is positive for $x < 0$ and negative for $x > 0$ and

$$\Theta(x) = \frac{T(x)-T_s-\frac{E^2 t_s t}{\rho k_s}}{T_0-T_s-\frac{E^2 t_s t}{\rho k_s}} \text{ and } Q_{GB} = \frac{\frac{E^2 \ell_{eff}^{\,2}}{\rho_{GB} k}}{T_0-T_s-\frac{E^2 t_s t}{\rho k_s}} \tag{S9}$$

where t_s is the insulating substrate thickness (here 90 nm SiO_2), $t = 0.34$ nm is the graphene thickness, k_s =1.4 $Wm^{-1}K^{-1}$ is the SiO_2 substrate thermal conductivity, and k = 300 $Wm^{-1}K^{-1}$ is the graphene thermal conductivity (here encased between SiO_2 and PMMA).[14] The thermal healing length[15] $L_H = (k\times t\times t_s/k_s)^{1/2}$ is approximately 80 nm for our geometry.

Equation S10 yields the percent increase in GB temperature $T_{\%} = T_{GB}/T(L/2)$ relative to the graphene sheet. The GB temperature rise T_{GB} is divided by the temperature rise at $T(L/2)$, halfway between the GB and contacts. To derive Eq. S10 we assume $T_s = T_0 = 0$ K and $L_H \ll L$.

$$T_{\%} = \frac{2e^{-L/L_H} + 0.5Q_{GB}L_H - 1}{e^{-L/(2L_H)} - 1} \tag{S10}$$

VII-B. Verification of Analytical Model

A FEA model of the device in Figure 4(a) was developed to verify Equations S6-S10. The FEA and analytical model yield the same results for Equations S6 and S7. The FEA and analytical model yield similar results for Equations S8 and S10. The predicted $T(x)$ of the FEA and analytical model deviate slightly at the contacts and GB as the FEA model accounts for 2D heat spreading in the substrate. Lateral substrate heat spreading is significant within a few L_H of the GB and contacts. The analytical model does not account for lateral substrate heat spreading, overestimates T_{GB} by 20-50 %, and is an upper bound of the predicted $T_{\%}$.

VIII. Thermal Measurements of Grain Boundaries

The measurement column of Table I lists the measurement technique used to measure the GB resistivity ρ_{GB}. For high ρ_{GB} ($\geq 10^3$ Ω μm) electrical (resistive) based measurements are able to measure ρ_{GB}, as the GB resistance R_{GB} and GB voltage drop V_{GB} are large.[12,13] For low ρ_{GB} (≤ 100 Ω μm) electrical measurements are unable to measure ρ_{GB}, as V_{GB} and R_{GB} are small[11] and only electrically based scanning tunneling microscopy (STM) measurements have been able to observe low resistivity GBs.[1] Low ρ_{GB} GBs do not significantly affect graphene electrical performance, particularly for longer devices (e.g. >5 μm).[11] However, we have shown the GB temperature rise can be large for low ρ_{GB} devices. The large GB temperature rise is due to highly local Joule heating at the GB. Recent work has estimated the GB influences <10 nm of the surrounding graphene,[16] and even a low V_{GB} will cause significant and highly localized Joule heating across such a small area. Therefore, nanometer-scale based thermometry methods, such as scanning thermal microscopy (SThM)[17] and SJEM,[5,6,18] have potential to study graphene GBs due to the large temperature rise at the GB.

IX. Raman Measurements

Figure S6 shows a typical Raman spectrum of the graphene used in this study. We note a large amorphous carbon baseline at ~1100-1500 cm^{-1} due to unstitched areas of carbon, wrinkles in the graphene grain, or leftover polymer residue from the transfer which carbonized during the anneal. The amorphous carbon baseline was present on other samples transferred with PMMA, poly(bisphenol A carbonate), and poly(lactic acid) (PLA) scaffolds.[19] The baseline persists on all samples, regardless of the transfer scaffold used, suggesting that it originates during the CVD growth process. Regardless, the presence of the amorphous carbon baseline does not allow us to determine quantitatively if the graphene is monolayer from solely the 2D/G peak ratio [I(2D)/I(G)]. Therefore, we measured the full width at half maximum (FWHM) of the 2D band and found it to be ~25 cm^{-1} which implies the graphene is monolayer.[20] We also do not observe a pronounced nucleation point from our Raman scans, which would indicate bilayer graphene, or additional optical absorption peaks from turbostratic graphene. These observations support the conclusion that the graphene is monolayer.

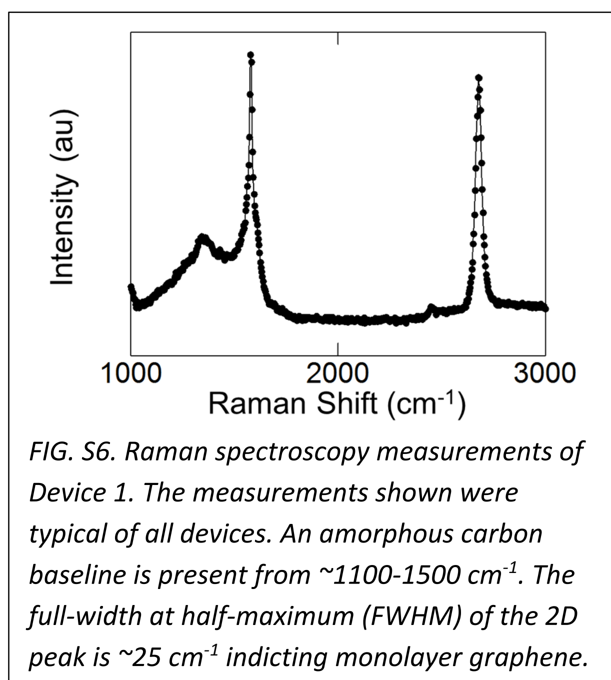

FIG. S6. Raman spectroscopy measurements of Device 1. The measurements shown were typical of all devices. An amorphous carbon baseline is present from ~1100-1500 cm^{-1}. The full-width at half-maximum (FWHM) of the 2D peak is ~25 cm^{-1} indicting monolayer graphene.

Supplemental References

1. K.W. Clark, X.G. Zhang, I.V. Vlassiouk, G. He, R.M. Feenstra, and A.-P. Li, ACS Nano **7**, 7956 (2013).
2. I. Vlassiouk, P. Fulvio, H. Meyer, N. Lavrik, S. Dai, P. Datskos, and S. Smirnov, Carbon **54**, 58 (2013).

[3] X. Liang, B.A. Sperling, I. Calizo, G. Cheng, C.A. Hacker, Q. Zhang, Y. Obeng, K. Yan, H. Peng, Q. Li, X. Zhu, H. Yuan, A.R. Hight Walker, Z. Liu, L.-m. Peng, and C.A. Richter, ACS Nano **5**, 9144 (2011).
[4] Y. Dan, Y. Lu, N.J. Kybert, Z. Luo, and A.T.C. Johnson, Nano Letters **9**, 1472 (2009).
[5] K.L. Grosse, M.-H. Bae, F. Lian, E. Pop, and W.P. King, Nature Nanotech. **6**, 287 (2011).
[6] K.L. Grosse, F. Xiong, S. Hong, W.P. King, and E. Pop, Appl. Phys. Lett. **102**, 193503 (2013).
[7] J. Martin, presented at the the COMSOL Conference, Hannover, Germany, 2008 (unpublished); E.M. Lifshitz, L.D. Landau, and L.P. Pitaevskii, *Electrodynamics of Continuous Media*. (Butterworth-Heinemann, 1984).
[8] M.-H. Bae, Z.-Y. Ong, D. Estrada, and E. Pop, Nano Letters **10**, 4787 (2010).
[9] N.F. Martinez, S. Patil, J.R. Lozano, and R. Garcia, Appl. Phys. Lett. **89**, 153115 (2006).
[10] B. Jabakhanji, A. Michon, C. Consejo, W. Desrat, M. Portail, A. Tiberj, M. Paillet, A. Zahab, F. Cheynis, F. Lafont, F. Schopfer, W. Poirier, F. Bertran, P. Le Fèvre, A. Taleb-Ibrahimi, D. Kazazis, W. Escoffier, B.C. Camargo, Y. Kopelevich, J. Camassel, and B. Jouault, Phys. Rev. B **89**, 085422 (2014).
[11] P.Y. Huang, C.S. Ruiz-Vargas, A.M. van der Zande, W.S. Whitney, M.P. Levendorf, J.W. Kevek, S. Garg, J.S. Alden, C.J. Hustedt, Y. Zhu, J. Park, P.L. McEuen, and D.A. Muller, Nature **469**, 389 (2011).
[12] L.A. Jauregui, H. Cao, W. Wu, Q. Yu, and Y.P. Chen, Solid State Commun. **151**, 1100 (2011); Q. Yu, L.A. Jauregui, W. Wu, R. Colby, J. Tian, Z. Su, H. Cao, Z. Liu, D. Pandey, D. Wei, T.F. Chung, P. Peng, N.P. Guisinger, E.A. Stach, J. Bao, S.-S. Pei, and Y.P. Chen, Nat Mater **10**, 443 (2011).
[13] A.W. Tsen, L. Brown, M.P. Levendorf, F. Ghahari, P.Y. Huang, R.W. Havener, C.S. Ruiz-Vargas, D.A. Muller, P. Kim, and J. Park, Science **336**, 1143 (2012).
[14] J.H. Seol, I. Jo, A.L. Moore, L. Lindsay, Z.H. Aitken, M.T. Pettes, X. Li, Z. Yao, R. Huang, D. Broido, N. Mingo, R.S. Ruoff, and L. Shi, Science **328**, 213 (2010); W. Jang, Z. Chen, W. Bao, C.N. Lau, and C. Dames, Nano Letters **10**, 3909 (2010).
[15] D.D. Frank Incopera, Bergman, Lavine, *Fundamentals of Heat and Mass Transfer*, 6 ed. (John Wiley and Sons, 2007).
[16] J.C. Koepke, J.D. Wood, D. Estrada, Z.-Y. Ong, K.T. He, E. Pop, and J.W. Lyding, ACS Nano **7**, 75 (2013).
[17] D.G. Cahill, P.V. Braun, G. Chen, D.R. Clarke, S. Fan, K.E. Goodson, P. Keblinski, W.P. King, G.D. Mahan, A. Majumdar, H.J. Maris, S.R. Phillpot, E. Pop, and L. Shi, Appl. Phys. Rev. **1** (2014).
[18] J. Varesi and A. Majumdar, Appl. Phys. Lett. **72**, 37 (1998).
[19] J.D. Wood, S.W. Schmucker, R.T. Haasch, G.P. Doidge, L. Nienhaus, G.L. Damhorst, A.S. Lyons, M. Gruebele, R. Bashir, E. Pop, and J.W. Lyding, presented at the Nanotechnology (IEEE-NANO), 2012 12th IEEE Conference on, 2012, DOI: 10.1109/NANO.2012.6322101.
[20] A.C. Ferrari, J.C. Meyer, V. Scardaci, C. Casiraghi, M. Lazzeri, F. Mauri, S. Piscanec, D. Jiang, K.S. Novoselov, S. Roth, and A.K. Geim, Physical Review Letters **97**, 187401 (2006); A.C. Ferrari and D.M. Basko, Nat Nano **8**, 235 (2013).